Physics-based Computational Modeling and Time-resolved Imaging of Plasma Plume Generated by Nanosecond Laser Interaction with a Bed of Micro Metallic Powder

Hanyu Song, Weidong Liu and Benxin Wu*

School of Mechanical Engineering, Purdue University, West Lafayette IN, USA

Abstract: Although continuous lasers see frequent applications in selective laser melting or sintering, lasers with short pulse durations (such as those with nanosecond scale durations) possess potential advantages that may include good spatial resolutions and small heat-affected zones. Previous work on selective laser sintering with nanosecond lasers has been reported, particularly for laser micro sintering. At a sufficiently high intensity, a nanosecond (ns) laser pulse can generate a plasma plume from its irradiated metallic powder bed surface. The plasma plume evolution, such as the pressure it generates on the surface of the powder bed, may significantly influence the sintering process in the powder bed. However, physics-based modeling work for plasma generated by nanosecond-pulsed laser interaction with a metallic micro powder bed has been seldomly seen in literatures according to the knowledge of the authors'. Such modeling work has been reported in this paper for a ~4-ns laser pulse interaction with a cobalt micro powder bed, integrated with time-resolved plasma imaging using an intensified CCD (ICCD) camera with nanosecond scale gate widths for the model validation. For the conditions investigated, the model-predicted plasma plume evolutions agree reasonably well with the ICCD imaging results for the given period of comparison. This has reasonably supported the hypothesis posed in this paper (which has been rarely tested according to the knowledge of the authors') that a short ns laser pulse-induced plasma from a metallic micro powder bed below the critical temperature can be reasonably well described by solving gas dynamic equations in the gaseous phase together with solving the heat transfer equation in the powder bed condensed phase, where the coupling is via the Knudsen layer (KL) relations for vaporization at the interface between the two phases. The model calculations show that in comparison with the bulk cobalt situation, the ns laser pulse can induce more significant surface vaporization from the cobalt powder bed, leading to a plasma plume with typically higher peak temperatures and densities in the simulated period. The plume can generate a short total pressure pulse with a ~491-MPa peak magnitude on the surface of the powder bed.

Keywords: selective laser melting, laser micro sintering, selective laser sintering

1. Introduction

Lasers are powerful tools for additive manufacturing. The layer-by-layer selective laser melting or sintering process (SLM or SLS) can rapidly produce parts with complicated shapes and

^{*} Corresponding author: Benxin Wu, Associate Professor, School of Mechanical Engineering, Purdue University, 585 Purdue Mall, West Lafayette, IN 47907, USA, email: wu65@purdue.edu

various compositions [1, 2], and have many current or potential industrial applications [3]. In SLS and SLM, continuous wave lasers are often employed [4, 5]. On the other hand, lasers with short pulse durations can also be used in SLS or SLM, which may possess potential advantages that may include good spatial resolutions and narrow heat affected regions. Studies on selective laser sintering with pulsed lasers have been reported, particularly for laser micro sintering (which is a process to produce micro scale features) [6, 7]. Out of lasers with different pulse durations, nanosecond lasers are often good choices for laser micro sintering, because they can have a strong overall competitiveness combining relatively low costs (typically much lower than picosecond and femtosecond lasers for getting the same average power), strong robustness, short pulse durations, and high achievable average and transient powers. Laser micro sintering work using nanosecond lasers has been reported in the literature, such as [6-9] (in this paper, for simplicity, the term "laser sintering" will be employed to represent all laser-generated powder coalition processes regardless of the extent of melting). The costs of nanosecond lasers have been decreasing, which are expected to see more and more potential applications in additive manufacturing.

For nanosecond-pulsed laser sintering of a metallic powder, if the laser intensity is sufficiently large, then the laser irradiation could generate strong vaporization from the surface of the powder bed, forming a plasma plume, whose generation and evolution can greatly affect the laser sintering process. For example, due to the plasma, a high pressure pulse can be induced on the surface of the powder bed. This can help condense the powder bed [6], promote molten metal flow, decrease balling and/or increase densification of sintered material [8, 9]. Hence, it is very

important to fundamentally understand the plasma plume evolution generated by nanosecond laser interaction of a metallic powder bed.

To obtain a thorough understanding of such a complicated process, it is desirable to perform an integrative study, combining physics-based computational modeling with time-resolved observations of the plasma. The experimental results can help validate the model, while the validated model can help produce an in-depth and continuous physical picture of the process that is difficult to obtain via experiments alone. However, to the authors' knowledge, such an integrative study has been rarely reported. In particular, physics-based modeling work for plasma generated by nanosecond laser interaction with a metallic micro powder bed has been seldomly seen in the literature to the authors' knowledge, although modeling studies have been reported for nanosecond laser-induced plasma from a bulk target of metal or semiconductor (e.g., [10, 11]).

Ref. [12] reported experimental study of plasma induced in Q-switched pulsed YAG laser micro sintering of copper-based powder (where the Q-switching rate and duration are typically in the \sim kHz and \sim μ s scale, respectively). Images of the plasma were taken using an ICCD camera. The plasma optical emission spectra were measured by a spectrometer, based on which the plasma temperatures and electron densities are deduced. Ref. [13] reported a time-resoled imaging study for nanosecond laser pulse interactions with metal micro particles (whose diameters are on the scale of \sim 30 μ m) sitting on a transparent substrate. The imaging study shows the plasma plume expansion, shock wave propagation and the melted material ejection induced by the interactions. Ref. [14] studied the optical emission of the plasma generated by nanosecond laser ablation of

randomly packed copper spheres with diameters in the range of 49 to 390 μ m, and the study revealed a steplike phenomenon in the relation between the plasma emission strength and the microsphere diameter.

Despite the experimental studies listed above, a *physics-based modeling* study for plasma generated by nanosecond laser interaction with a metallic micro-powder bed has been rarely seen in the literature to the authors' knowledge. Ref. [15] reported high-speed imaging results and a finite element model for laser powder bed fusion (PBF) that considered the laser-induced plume; but the study is for CW laser-powder bed interactions, not those induced by a nanosecond laser.

In some previous studies (e.g., [10, 11]), plasma generated by nanosecond-pulsed laser irradiation of a bulk target has been modeled by solving gas dynamic equations in the gaseous phase and solving the heat transfer equation in the target condensed phase, where the equations are coupled via the Knudsen layer relations for evaporation from the surface of the condensed phase. The model-predictions agree reasonably well with time-resolved plasma imaging results [10, 11]. To the authors' knowledge, further work is still needed to verify whether or not the previous modeling approach for nanosecond laser-induced plasma from a bulk target can also be employed to reasonably accurately model nanosecond laser-induced plasma from a metallic micropowder bed if the powder bed effective properties are used.

To fill this knowledge gap, in this paper it is hypothesized that a modeling approach similar to that described above can also provide a good description of the plasma evolution generated by short nanosecond-scale laser pulse interaction with a metallic micro-powder bed (if the powder

bed surface temperature is below the metallic material thermodynamic critical temperature and if surface vaporization is the main mechanism for the plasma generation). In this paper, the hypothesis will be tested via an integrative modeling and experimental study. If this hypothesis was tested and supported, it would contribute important new knowledge to the field and help build a critical scientific basis for modeling the evolutions of such plasma under similar conditions, which could play an important role in nanosecond laser sintering with parameters that can generate plasma.

In this paper, to test the aforementioned hypothesis, physics-based modeling work, integrated with time-resolved imaging, has been performed for plasma generated by the interaction of a very short nanosecond laser pulse with a metallic (cobalt) micro-powder bed. In the model, compressible gas dynamic equations are solved for the metal vapor and air, while the heat transfer equation is solved for the powder bed condensed phase. Compared with a bulk metal, one important difference of a metal powder bed is that it can have significantly different effective properties, such as effective thermal conductivity and density. Hence, in the model, the effects of the powder bed porosity on the medium effective thermal conductivity and density have been considered. The Knudsen layer relations for surface vaporization are employed to connect the aforementioned governing equations in the gaseous and condensed phases. Images of the laser-induced plasma are taken using an ICCD camera with nanosecond-scale gate widths for a high resolution in time. An objective and a tube lens are positioned in front of the ICCD camera to obtain a microscale spatial resolution for the imaging. The time-resolved imaging results are used

to validate the model and test the aforementioned hypothesis. Modeling and time-resolved imaging work is also conducted for plasma generated by nanosecond laser interaction with a bulk cobalt target. The study has revealed the differences between the plasma evolution from the metal powder bed and that from the bulk metal target induced by a ns laser pulse with the same parameters under the conditions investigated.

In laser micro sintering, small particles on the scale of a few μ m or less could benefit spatial resolutions and were often used (e.g., [6, 7]). Hence, in this paper small particles with a nominal size of ~1.6 μ m have been used. The gained knowledge from the work in this paper will benefit the field of laser micro sintering, where nanosecond lasers are often employed.

2. Model

Figure 1 shows the schematic diagram for the two-dimensional (2D) axisymmetric model. Based on the hypothesis described in the *Introduction* section, the modeling approach employed and demonstrated in Fig.1 is similar to those employed in the corresponding author's prior papers in [10, 11] for plasma plume due to surface evaporation generated by nanosecond-pulsed laser irradiation of a bulk metal or silicon target. In the current paper, however, the powder bed properties, which could be very different from those for the bulk metal, will be used. As shown and discussed later, the property difference can cause very different plasma evolutions. The comparison of the model predictions with the time-resolved imaging results for the plasma evolution can test the hypothesis posed in the *Introduction* section under the conditions

investigated. That is, a short nanosecond laser pulse-induced plasma from a metallic micro-powder bed below the critical temperature can be reasonably well described by solving the compressible gas dynamic equations in the gaseous phase together with solving the heat transfer equation in the powder bed condensed phase, where the coupling is via the Knudsen layer relations for vaporization from the surface of the condensed phase.

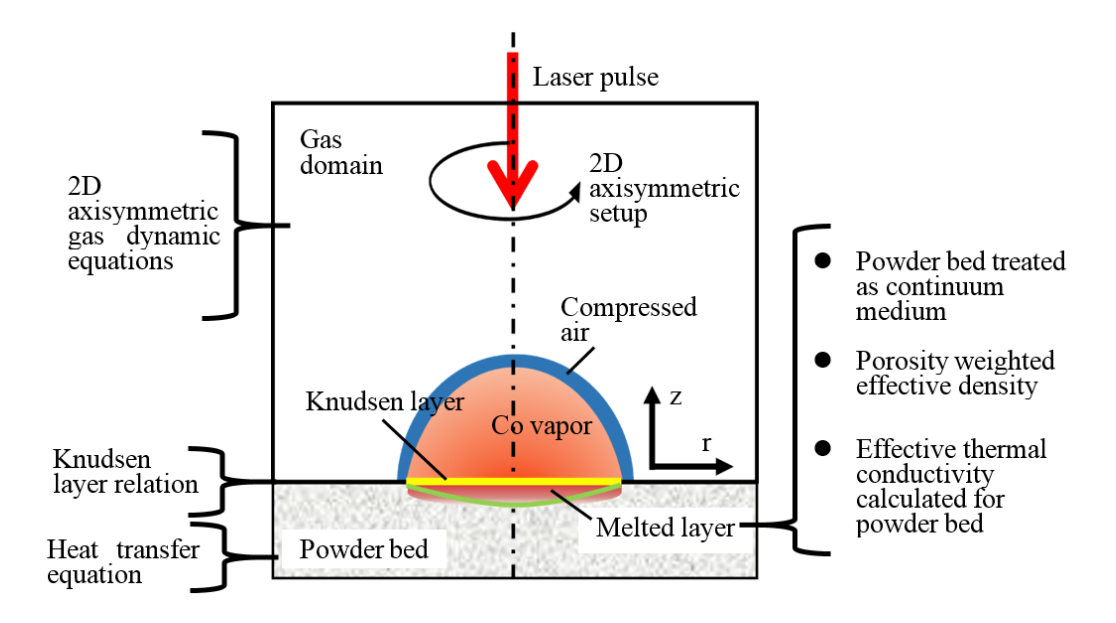


Figure 1. The schematic diagram of the model for plasma generated by the interaction of a nanosecond laser pulse with a metallic micro-powder bed.

In the model, the laser beam is assumed to propagate downwards along the direction of -z and irradiate at the surface of the powder bed located at z = 0. A layer in the surface of the cobalt micro-powder bed may be melted, and at sufficiently high surface temperatures, significant surface vaporization may take place. The vaporization-induced material removal may cause a small receding velocity of the powder bed surface in the -z direction with a magnitude of V_{rec} . If the

original point of the z axis is defined to be fixed at the powder bed surface, then in this coordinate system, the powder bed will have a velocity of the same magnitude in +z direction, V_{rec} . Then the heat transfer process in the powder bed condensed solid and liquid phases is assumed to be governed by the following equation [11, 16-20]:

$$\rho_{eff} \frac{\partial H}{\partial t} + \rho_{eff} V_{rec} \frac{\partial H}{\partial z} = \frac{\partial}{\partial z} \left(k' \frac{\partial T}{\partial z} \right) + \frac{1}{r} \frac{\partial}{\partial r} \left(rk' \frac{\partial T}{\partial r} \right) + \frac{\partial I_{laser}(r, z, t)}{\partial z}$$
(1)

where t and T denote time and temperature, respectively, $I_{laser}(r,z,t)$ is the laser beam intensity, r and z denote spatial coordinates, ρ_{eff} is the powder bed medium effective density given by $\rho_{eff} = (1-\alpha)\rho_{bulk}$ (where ρ_{bulk} is the bulk metal density and α is the powder bed porosity), k' is the effective powder-bed-medium thermal conductivity, and the enthalpy (per unit mass) H is related to the temperature via the following relation:

$$H_{0} + \int_{T_{0}}^{T} C_{p,s} dT , \qquad \qquad for: \ T \leq T_{m} - \Delta T$$

$$H(T) = H(T_{m} - \Delta T) + \frac{T - (T_{m} - \Delta T)}{2\Delta T} h_{m}, \qquad for: \ T_{m} - \Delta T < T \leq T_{m} + \Delta T \qquad (2)$$

$$H(T_{m} + \Delta T) + \int_{T_{m} + \Delta T}^{T} C_{p,l} dT , \qquad for: \ T > T_{m} + \Delta T$$

where T_m represents the melting point, $C_{p,s}$ and $C_{p,l}$ denote the solid and liquid metal specific heat, respectively, h_m is the melting latent heat, H_0 is the enthalpy at T_0 , and ΔT is a small temperature range value (0.5 K is used in this study).

The metal powder bed medium and the corresponding bulk metal can have very different thermal conductivities. For the experimental work reported in this paper, the initial solid powder bed porosity was approximately estimated to be around ~0.72 through the measured powder apparent density. In Ref. [21], by numerical modeling of the heat transfer process for micro metal particles filled stochastically in the computational domain, the effective thermal conductivity for

a powder bed of solid iron micro particles with various porosity values is obtained. It shows that the powder bed of solid micro iron particles in air with a porosity near ~ 0.72 has an effective thermal conductivity about ~3% of that for the bulk iron. The regular density, specific heat and thermal conductivity of a solid iron are reasonably similar to the values for a solid-state cobalt [21-24]. Hence, based on the result in [21], in this paper an approximate assumption has been made that the effective solid-state cobalt powder-bed medium thermal conductivity is given by: k' = $0.03k_{b,sol}$, where $k_{b,sol}$ denotes the solid-state bulk cobalt thermal conductivity. For the molten medium of the powder bed above $T_m + \Delta T$, its effective conductivity is simply estimated by k' = $(1-\alpha)k_{b,liq} + \alpha k_g$ [25], where $k_{b,liq}$ and k_g are the conductivity of the liquid bulk cobalt and the gaseous material filling the pores, respectively. The value of k_g is expected to be much smaller than $k_{b,liq}$ and hence is neglected, leading to $k' = (1 - \alpha)k_{b,liq}$. The thermal conductivity of the melted and re-solidified powder bed medium is calculated by $k' = (1 - \alpha)k_{b,sol}$. The total simulated time duration in this paper is very short (tens of nanoseconds), and the melted powder bed medium is assumed to remain at the same effective density (ρ_{eff}) as that for the solid-state powder bed medium during the simulated duration. Based on this assumption, the melted powder bed medium porosity can be deduced using the solid-state bulk cobalt density, the liquid bulk cobalt density and the initial solid cobalt powder bed porosity.

The major purpose of the model in this paper is to simulate the plasma evolution induced by a very short (~4 ns) laser pulse interaction with a metallic micro-powder bed. Due to the small sizes and large number of particles involved, it would be computationally extremely expensive (if

feasible at all) to discretize the space of each and every particle into many small cells for numerical calculations. Hence, the powder bed has been approximately treated as a continuum medium with effective properties (e.g., the effective conductivity and mass density as previously introduced). The condensed-phase portion of the model is mainly to capture the dominant physical processes related to surface vaporization from the laser-induced molten metal in the powder bed, which leads to the plasma plume generation. If the laser beam is treated as being composed of many light rays with finite but very small individual cross sections, then each light ray would most likely be intercepted by a certain particle in the surface layer of the powder bed. A portion of the power of the light ray will be absorbed in a very thin surface layer of the particle and the layer thickness is on the scale of $\sim 1/\beta_b$, where β_b is the bulk cobalt optical absorption coefficient and it is related to the imaginary part of the complex refractive index n_i by $\beta_b = \frac{4\pi n_i}{1064 \text{ nm}}$ [26]. The layer thickness is very small and on the scale of only ~15 nm. This factor, together with the short duration (~4 ns) and high intensity of the laser pulse in the studied condition, can lead to a very high absorbed laser power density per unit volume (the $\partial I_{laser}/\partial z$ term in Eq.(1)) for the particle surface layer. As a result, a thin molten metal layer with very high surface temperatures may be very quickly generated (within a short time scale that is expected to be only a few ns), leading to a rapid surface vaporization from the molten metal layer. This will cause the plasma formation and fast expansion above the powder bed surface.

Thus, under the conditions studied, a key factor related to the rapid vaporization and fast plasma expansion from the laser-irradiated powder bed (as shown later in the ICCD imaging

results) is the large bulk cobalt optical absorption coefficient (and thus small absorption depth), leading to a very high absorbed laser power density per unit volume for the surface layer of each particle intercepting the small light ray. To capture this, in the model in this paper, the laser energy absorption in the powder bed is calculated using the bulk cobalt optical properties at 1064 nm. That is, the surface optical reflectivity and the optical absorption coefficient of the powder bed for the laser beam is calculated based on the complex index of refraction for the cobalt, $n_r + in_i$, at 1064 nm via the Fresnel equations and the relation: $\beta_b = \frac{4\pi n_i}{1064 \text{ nm}}$, respectively [26].

A very strict way to numerically model the laser interaction with the powder bed should be to discretize the space of each and every particle into many small cells and numerically solve the related governing equations (including those for laser propagation and for heat transfer). However, this would be computationally extremely expensive (if feasible at all) due to the large number of particles involved. Hence, the simplified approach as described in this paper is used, which has an acceptable computational cost. Whether or not this approach can provide a reasonably good description of the plasma evolution under the conditions studied will be teste by comparing the predictions from the model with the time-resolved imaging results for the plasma as shown later.

The metal (cobalt) vapor leaving the powder bed surface may have high temperatures and pressures. It will push the ambient air, generating a compressible gas dynamic flow process in the gaseous phase (vapor and air) that can be assumed to be governed by the following gas dynamic equations [10, 11, 20, 27-29]:

$$\frac{\partial \rho_{vap}}{\partial t} + \frac{\partial (\rho_{vap} U_r)}{\partial r} + \frac{1}{r} (\rho_{vap} U_r) + \frac{\partial (\rho_{vap} U_z)}{\partial z} = 0$$
 (3a)

$$\frac{\partial \rho_{air}}{\partial t} + \frac{\partial (\rho_{air} U_r)}{\partial r} + \frac{1}{r} (\rho_{air} U_r) + \frac{\partial (\rho_{air} U_z)}{\partial z} = 0$$
 (3b)

$$\frac{\partial \rho U_r}{\partial t} + \frac{\partial \rho U_r^2}{\partial r} + \frac{1}{r} (\rho U_r^2) + \frac{\partial (\rho U_r U_z)}{\partial z} = -\frac{\partial p}{\partial r}$$
(3c)

$$\frac{\partial \rho U_z}{\partial t} + \frac{\partial \rho U_r U_z}{\partial r} + \frac{1}{r} (\rho U_r U_z) + \frac{\partial (\rho U_z^2)}{\partial z} = -\frac{\partial p}{\partial z}$$
 (3d)

$$\frac{\partial(0.5\rho U^2 + E_{int})}{\partial t} + \frac{\partial[(0.5\rho U^2 + E_{int} + p)U_r]}{\partial r} + \frac{1}{r}(0.5\rho U^2 + E_{int} + p)U_r + \frac{\partial[(0.5\rho U^2 + E_{int} + p)U_z]}{\partial z} = \frac{\partial}{\partial z}\left(k_{gas}\frac{\partial T}{\partial z}\right) + \frac{1}{r}\frac{\partial}{\partial r}\left(rk_{gas}\frac{\partial T}{\partial r}\right) + \beta I_{laser}$$
(3e)

where ρ_{vap} , ρ_{air} , ρ represent the metal vapor, air and total density, respectively, U_r , U_z and U denote the r-, z-direction and the total speed, respectively, E_{int} and p are the internal energy per unit volume and pressure, respectively, and k_{gas} and β represent the thermal conductivity and optical absorption coefficient (at the laser beam wavelength) of the gaseous phases, respectively. The wavelength of the laser beam used in this study is ~1064 nm, and it has been assumed that the vapor plasma absorption of the laser beam is mainly through the electron-ion inverse bremsstrahlung process, based on which the optical absorption coefficient is given by [30]:

$$\beta = \sum_{z_c} \frac{4}{3} \left(\frac{2\pi}{3k_b T} \right)^{0.5} \frac{n_e n_{z_c} z_c^2}{h c m_e^{1.5}} \frac{e^6}{(4\pi \nu \varepsilon_0)^3} \left(1 - e^{-\frac{h\nu}{k_b T}} \right)$$
(4)

where k_b and h denote the Boltzmann and Planck constants, respectively, c and v denote the vacuum light speed and the laser light frequency, respectively, n_{z_c} and n_e denotes the ion and free electron number density, respectively, m_e is the electron mass, ε_0 and e represent the vacuum permittivity and the charge of an electron, respectively, and z_c denotes the ionic charge number.

For Eq.(4), one to three-fold ionized atoms are considered because the number density of further ionized atoms is very small. The thermal conductivity is given by [31]:

$$k_{gas} = k_{air}, for the air region k_b n_e \sqrt{\frac{8k_b T}{\pi m_e}} \frac{1}{(2+\sqrt{2})n_e A_{ei} + 2n_a A_{ea}}, for the vapor region$$
 (5)

where k_{air} is the air thermal conductivity, n_a is the neutral vapor atom number density, and A_{ea} and A_{ei} represent the cross sections for the electron-neutral atom and electron-ion collisions, respectively, with the former being neglected under the conditions simulated and the latter being given by [31]:

$$A_{ei} = 6\pi \left(\frac{z_c e^2}{12\pi\varepsilon_0 k_b T}\right)^2 \ln \left(\frac{12\pi}{z_c e^3} \frac{(\varepsilon_0 k_b T)^{1.5}}{n_e^{0.5}}\right)$$
(6)

In the vapor region, only the thermal conductivity associated with free electrons is considered. The second line of Eq.(5) is based on the assumption that the free electron number density is approximately equal to the total ion number density. This assumption should be reasonable for the simulated conditions in this study where a dominant fraction of the vapor ions in the plasma are Co¹⁺ ions. In the calculation with Eq.(6), only the Co¹⁺ ions are considered.

The solution of the gas dynamic equations needs equation of state (EOS) for the gaseous phases. For the cobalt vapor region that could be ionized due to the high temperatures, an EOS table (where each line lists the vapor internal energy, pressure, electron and ion number densities for a given temperature-density pair) is constructed by first calculating the densities of ions, free electrons and neutral atoms by solving the Saha equations [32, 33] (during which one to five-fold ionized atoms have been considered). Then, based on the number densities, the pressure and

internal energy per unit volume at each given density-temperature pair in the table can be calculated [32, 33]. The internal energy includes the atom/electron/ion kinetic energy, $1.5k_bT(n_e + n_a + n_{i,total})$, as well as the ionization energies of the ions, where $n_{i,total}$ is the total number density of all the ions [32]. The pressure is given by $p = k_b T(n_e + n_a + n_{i,total})$ [32]. For the air region, it has been found from the simulation results that under the simulated conditions in this paper typically the air region with high temperatures is very thin (typically just a few microns or less), where the temperatures are also not very high (typically less than ~6500 K) and thus should not cause a very significant air ionization considering that the first ionization energies for oxygen and nitrogen are very high (~13.62 and ~14.35 eV, respectively) [34, 35]. Hence, for the entire air region, the ideal gas EOS is used (assuming a regular air composition), the optical absorption coefficient for the laser beam is assumed to be zero, and the regular roomcondition (0.1 MPa and 300 K) air conductivity determined based on [36] is used in the model calculations. The air internal energy is assumed to be $2.5k_bTn_p$ [32], where n_p is the air molecular number density. These are certainly simplified assumptions, but it is expected that they should not cause a big effect on the simulation results.

It is assumed that the intensity of the original incoming laser beam, $I_0(r,t)$, has a Gaussian spatial distribution. The beam propagation in the -z direction in the gaseous phase is assumed to be governed by $\frac{\partial I_{laser}(r,z,t)}{\partial (-z)} = -\beta I_{laser}$, where β denotes the optical absorption coefficient for the gaseous phase. For the condensed phase-gaseous phase interface at z=0, it is assumed that: $I_{laser}(r,z=0^-,t)=(1-R)I_{laser}(r,z=0^+,t)$, where R denotes the optical reflectivity of the

condensed phase surface. The further propagation of the laser beam into the condensed phase is assumed to be governed by $\frac{\partial I_{laser}(r,z,t)}{\partial (-z)} = -\beta_b I_{laser}$. In this way, the absorbed laser power density terms in Eqs.(1) and (3e) can be obtained. The laser parameters are introduced in the *Experiment* section of this paper later. The model calculation results indicate that for the conditions investigated, the laser energy absorption by the plasma is not very significant and hence the further propagation of the laser beam reflected back from the condensed phase surface is not calculated.

Similar to the author's previous papers [11], the gas dynamic equations for the gaseous phases have been solved using the essentially non-oscillatory (ENO) method introduced in [37], while the heat transfer equation for the powder bed condensed phase has been solved with the explicit finite difference method. At each numerical time step, the former and the latter equations are related via the Knudsen layer (KL) relations right above the condensed phase surface (where the involved saturation vapor pressure at the temperature of the condensed phase surface is calculated using the Clausius-Clapeyron equation) [11, 17, 18, 20, 38-41]. The KL relations are clearly described in Ref. [11]. Under the studied conditions, the model simulation results show that the plasma spatially peak temperature at each time step is typically less than 10000 K and the vapor ionization degree is relatively low. Hence, the effect of ionization is not considered in the KL relations. For the gaseous phase domain bottom boundary at z = 0, it is assumed that $U_r = 0$. The solution procedure at each time step is similar to that introduced in Ref.[11], where readers can find more details.

For the condensed phase domain, the mesh sizes in r and z directions are $\Delta r = 0.5 \mu m$

(uniform) and $\Delta z_{minimum} = 30$ nm, respectively. The value of Δz increases with |z| at an expansion ratio of 1.1 between adjacent numerical cells. For the gaseous phase domain, the mesh sizes in r and z directions are $\Delta r = 0.5 \,\mu m$ (uniform) and $\Delta z = 0.5 \,\mu m$ (uniform), respectively. The numerical time step is $\Delta t = 0.01$ ns. To verify the mesh sizes and time step used are sufficiently small, simulations have been conducted with coarser meshes or a larger time step, such as (1) $\Delta r = 1 \,\mu m$ for both the condensed and gaseous phases and $\Delta z = 1 \,\mu m$ for the gaseous phase; (2) $\Delta t = 0.02$ ns and (3) $\Delta z_{minimum} = 50$ nm for the condensed phase. The simulation results for the nanosecond-pulsed laser interaction with the powder bed (under the conditions in this paper) obtained with the different numerical parameters are very close. This implies that the numerical parameters used should be able to provide numerical accuracy and reliability sufficient for the purpose of this paper.

At t = 0, the powder bed and the ambient gas are assumed to have an initial temperature of 300 K, and the latter has an initial velocity of 0 and an initial pressure of 0.101 MPa. In the simulations, the domains for the powder bed (i.e., the condensed phase) and the gaseous phase are selected to be large enough such that for the model calculated period in this paper the conditions at the top, bottom and lateral boundaries of the entire domain can be reasonably assumed to stay at the initial conditions. The exact domain sizes are not critical as long as they are large enough. The gaseous phase domain size is 300 μ m × 300 μ m for the diameter and the size in z direction, respectively, while the condensed phase domain size is 300 μ m × 558 μ m. For the powder bed condensed phase surface, a boundary condition is applied based on energy balance, where the energy flux towards the surface is equal to that leaving the surface. The former includes the

condensed phase heat conduction and advection (due to V_{rec}) towards the surface. The latter includes the latent heat of vaporization, the internal and kinetic energy carried away by the vaporized material, the work done by pressure on the vapor, and the thermal radiation. It has been found that in the simulated conditions, the thermal radiation term does not significantly affect the model calculation results, and hence is calculated in an approximate way as: $\sigma(T_s^4 - 300^4)$, where σ denotes the Stefan-Boltzmann constant and T_s is the condensed phase surface temperature.

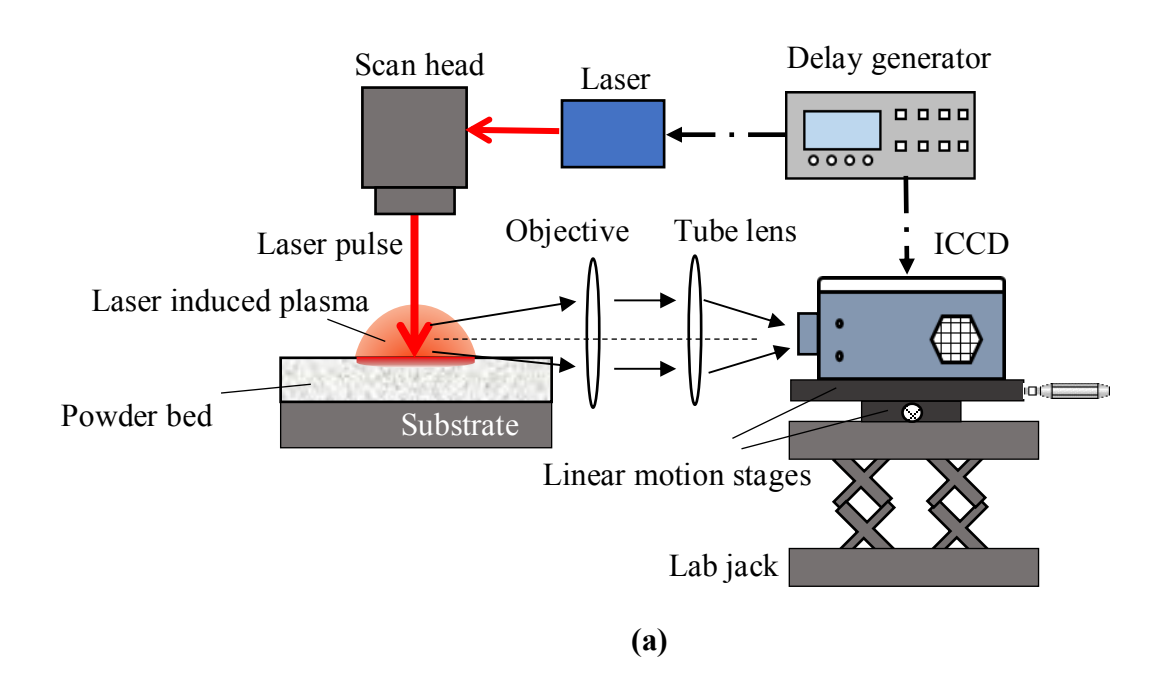
The main cobalt material properties utilized in the simulations are obtained from literatures [24, 42-48], for which the values and/or sources are listed in Table 1. As introduced earlier, the initial solid powder bed porosity has been experimentally measured to be approximately \sim 0.72. For the medium in the powder bed with temperatures in the range of $[T_m-\Delta T, T_m+\Delta T]$, the thermal conductivity, optical absorption coefficient and surface reflectivity are calculated through a linear interpolation utilizing the corresponding solid values at the temperature of $T_m-\Delta T$ and the melted liquid medium values at $T_m+\Delta T$.

As a comparison, the plasma induced by nanosecond laser pulse interaction with a bulk cobalt has also been modeled in a similar approach using the bulk cobalt properties.

3. Experiment

Figure 2a is a schematic diagram showing the experimental setup for this study, where the powder bed of cobalt particles in air is irradiated by a laser pulse of ~4 ns (full-width-at-half-maximum duration), which comes from the Onda laser (Bright Solutions) with the wavelength of

 \sim 1064 nm and is delivered onto the powder bed surface by the scan head (ScanLab, HurryScan 14) that contains a lens with a focal length equal to 100 mm. Figure 2b shows the temporal profile of the laser pulse measured with a photodiode. The laser pulse energy is measured to be \sim 0.21 mJ/pulse. The laser spot diameter on the powder bed surface is measured to be approximately \sim 100 μ m based on the knife edge method assuming the laser beam intensity has a Gaussian profile. The cobalt particles come from Alfa Aesar (Product number: 10455), which have a nominal particle size of \sim 1.6 μ m based on the product specification. In the experiment, cobalt powder particles are moistened by \sim 95% ethanol, and then spread into the powder bed via a doctor blade. The powder layer gets naturally dried before laser irradiation. The powder layer in the bed is thick enough such that it is expected that its bottom boundary does not affect the plasma evolution process in this study.



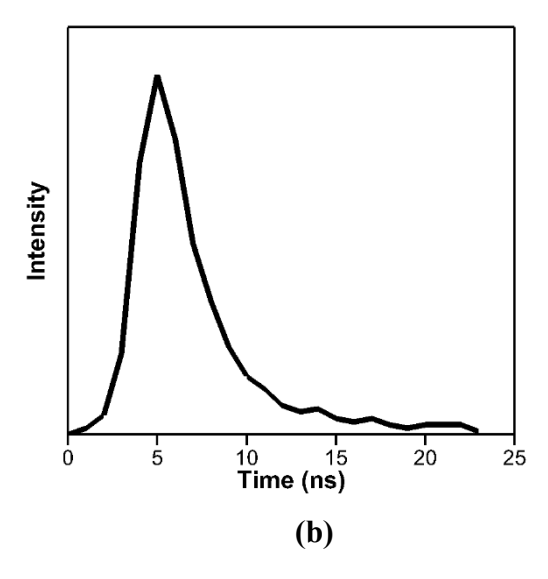


Figure 2. (a) Schematic of the experimental system for time-resolved imaging of the plasma generated by nanosecond laser interaction with a metallic micro-powder bed (the schematics given in this paper do not necessarily contain all the actual components or show them in an exact actual way. For example, the optics between the laser and the scan head are not shown), and (b) the laser pulse shape measured by a photodiode.

The plasma plume image is taken using an ICCD camera (Andor, iStar 334T). In this study, a gate width of 3 or 5 ns and a gain of 30 have been used for the ICCD camera. The ICCD camera is coupled with an objective lens and a tube lens to get a high spatial resolution. The camera has 1024×1024 active pixels, with a $\sim13~\mu m \times \sim13~\mu m$ pixel size. The objective and tube lens provide a 10-time spatial magnification. Hence, each pixel of the ICCD image corresponds to a region of $\sim1.3~\mu m \times \sim1.3~\mu m$ in the real physical domain. The ICCD camera and the laser are triggered by two different channels of a digital delay generator with a controlled delay time. By

changing the delay time, plasma images at different moments after the laser pulse beginning can be taken with the camera. The laser spot position will be changed to a new point on the powder bed after each laser pulse shot. As a comparison, images of plasma induced by the nanosecond laser pulse interaction with a bulk, polished cobalt (Sigma-Aldrich, 356891-6.25CM2, 1.0 mm-thick cobalt foil) have also been taken at different delay times.

4. Results and Discussions

Figure 3 shows the images of the plasma plume captured by the ICCD camera at various delay times after the cobalt powder bed irradiation by one laser pulse, in comparison with those for the plume induced from a bulk cobalt target. The moment at which the laser pulse begins is defined as the time of t = 0. It can be seen from Fig.3 that at $t = \sim 10$ ns, the plasma plume is already observable in the image for both the powder bed and the bulk metal situations. The plasma expands from $t = \sim 10$ to $t = \sim 30$ ns. In this period, the plasma plume induced from the powder bed is typically obviously larger than that from the bulk metal. Compared with that from the bulk cobalt, the faster expansion of the plasma plume from the cobalt powder bed in this period implies that likely the plasma plume has overall higher pressures, which also means higher temperatures and/or densities of the plume. It also suggests that likely the laser pulse has induced a more significant surface vaporization from the powder bed than that from the bulk metal.

For the ICCD images at $t = \sim 35$ ns, ~ 40 ns and ~ 45 ns, the visible portions of the plume appear to have reasonably similar sizes for the powder bed and the bulk metal situations. However,

the overall brightness levels of the plume from the powder bed appear much higher than those from the bulk metal in the images obtained with the same ICCD gain and gate width. Hence, the plume from the powder bed is expected to have a stronger optical emission, implying that it likely has overall higher temperatures and/or densities in the visible regions. At $t = \sim 55$ ns, the plume from the bulk metal is almost invisible in the ICCD image with the given gate width and gain. The plume from the powder bed is still visible in the images at $t = \sim 55$ ns and ~ 75 ns, which again indicates its stronger optical emission and likely overall higher temperatures and/or densities in the visible region than the plume from the bulk metal target.

In a short summary, the aforementioned comparison of the images for the plume from the powder bed with those from the bulk metal consistently indicate that the plume in the former situation likely have overall higher temperatures and/or densities than that in the latter situation.

Bulk metal $100 \mu m$ $t = 10 \text{ ns}$ Laser beam Metal surface	Bulk metal $\frac{100 \mu m}{t = 15 \text{ ns}}$	Bulk metal $\frac{100 \mu m}{t = 20 \text{ ns}}$	Bulk metal $\frac{100 \mu m}{t = 25 \text{ ns}}$
Powder bed $\frac{100 \mu m}{t = 10 \text{ ns}}$	Powder bed $100 \mu m$ $t = 15 \text{ ns}$	Powder bed $100 \mu m$ $t = 20 \text{ ns}$	Powder bed $100 \mu m$ $t = 25 \text{ ns}$
Bulk metal $\frac{100 \mu m}{t = 30 \text{ ns}}$	Bulk metal $\frac{100 \mu m}{t = 35 \text{ ns}}$	Bulk metal $\frac{100 \mu m}{t = 40 \text{ ns}}$	Bulk metal $\frac{100 \mu m}{t = 45 \text{ ns}}$
Powder bed $\frac{100 \mu m}{t = 30 \text{ ns}}$	Powder bed $\frac{100 \mu m}{t = 35 \text{ ns}}$	Powder bed $100 \mu m$ $t = 40 \text{ ns}$	Powder bed $100 \mu m$ $t = 45 \text{ ns}$
Bulk metal $100 \mu m$ $t = 55 \text{ ns}$	Bulk metal $\frac{100 \mu m}{t = 65 \text{ ns}}$		
Powder bed $ 100 \mu m $ $ t = 55 \text{ ns} $	Powder bed $\frac{100 \mu m}{t = 75 \text{ ns}}$	Powder bed $100 \mu m$ $t = 95 \text{ ns}$	Powder bed $\frac{100 \mu m}{t = 110 \text{ ns}}$

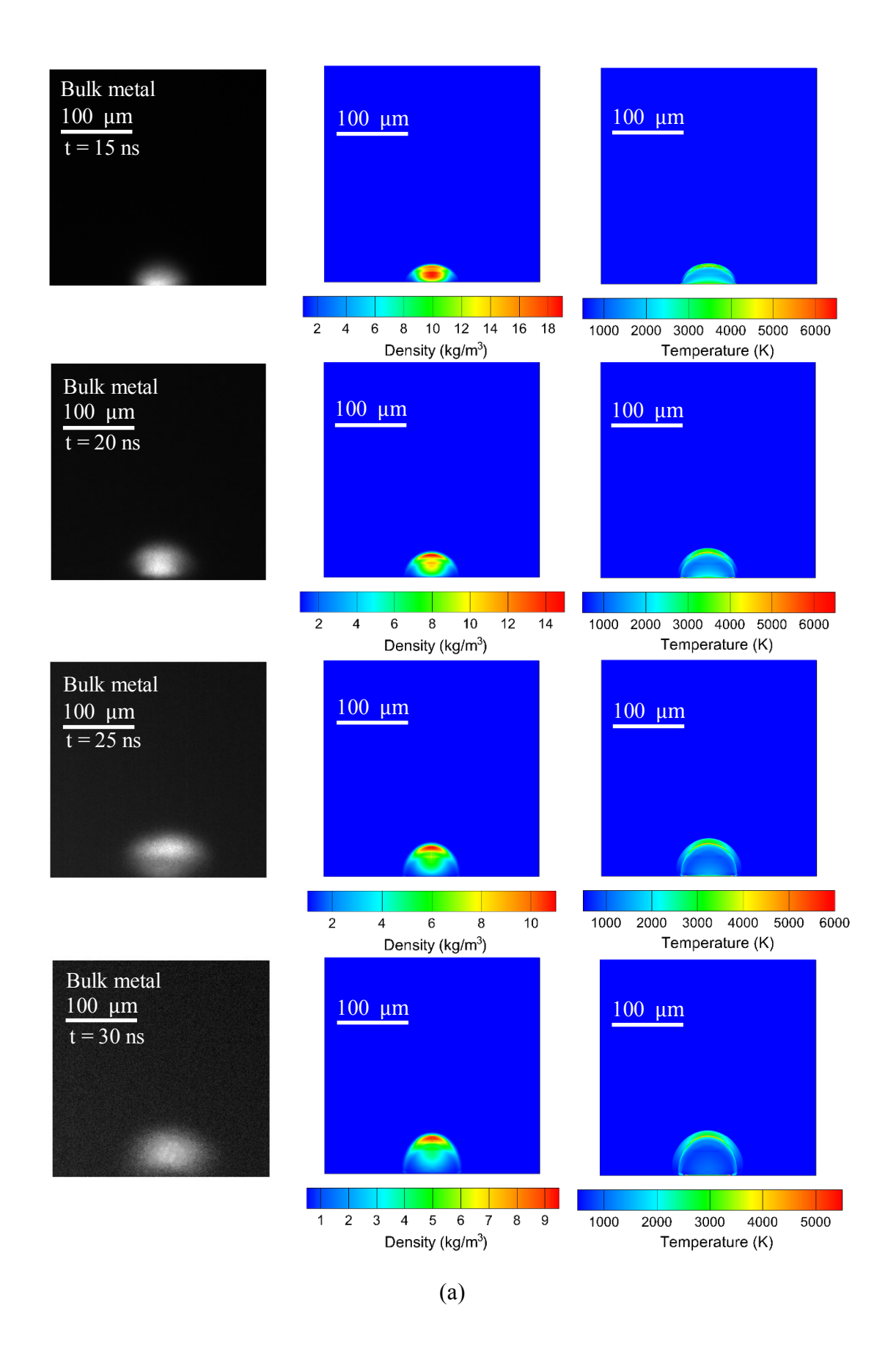
(continued from the previous page)

Figure 3. ICCD images of plasma plume generated by nanosecond-pulsed laser irradiation of a bulk cobalt target (odd lines) or a powder bed of micro cobalt particles (even lines) (ICCD gain: 30; gate width: 3 ns for t = 10 to 55 ns, and 5 ns for t = 65 ns to 110 ns. Laser pulse begins at t = 0. The approximate metal surface location is indicated in the first image.).

The laser pulse has a ~4-ns FWHM duration and the pulse intensity has already decreased to a very small value at $t = \sim 15$ ns as shown in Fig.2b. Without the laser energy input, the overall plume temperature and/or density may quickly drop as it expands. For the period of $t \le \sim 30$ ns, the plume in the given images has relatively high brightness levels and the plume front in the images quickly expands, indicating that the plume should have reasonably high optical emission intensities and the plume front showing up in the images should be reasonably close to its actual front, where the temperature has a relatively steep change. However, this is no longer the case for images at t = ~35 ns and later, where the brightness level drops a lot for the bulk metal situation, and the front showing up in the images does not significantly expand with time for both the powder bed and the bulk metal situations. This indicates that the plume front showing up in the images may or may not be the actual plume fronts. There might be a layer of gaseous material behind the actual plume front, which is not visible in the images because of its insufficient optical emission intensity (due to its insufficient temperature and/or density). Therefore, next only the plume images in the stage of $t \le \sim 30$ ns will be compared with the model predictions.

Figure 4a gives the ICCD images of the plume from the bulk metal in comparison with the model-predicted contours for the gaseous phase temperature and the cobalt vapor density. The figure has demonstrated that the plume top front locations shown in the ICCD images agree

reasonably well with those for the gaseous phase high temperature regions on the model-predicted contour plots. This can also be clearly seen in Fig.4b, which compares the plume top front locations deduced from the experiment (ICCD images) with those from the model simulation (which are the top front locations for the gaseous phase high-temperature region). The error bar for the experimental data represents the standard deviation of multiple measurements. The good model-experiment agreement in Fig.4 has reasonably supported that the modeling approach has provided a reasonably good description of the evolution of the plasma plume generated by laser irradiation of the bulk cobalt. This is consistent with the corresponding author's previous work, which shows that a similar modeling approach has provided simulation results for plasma generated by nanosecond laser irradiation of a bulk aluminum [10] or a bulk silicon [11] that agree reasonably well with in-situ time-resolved imaging results.



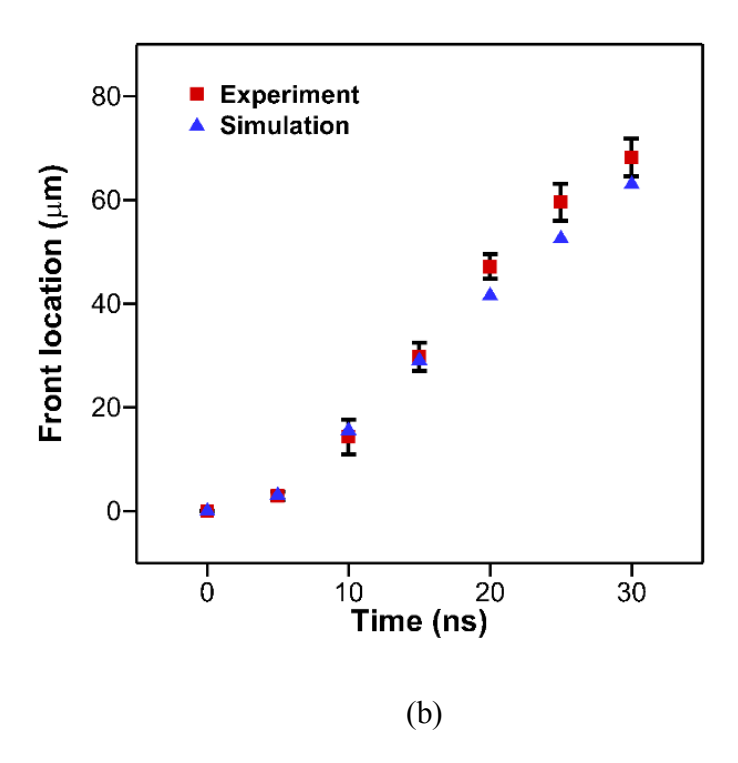
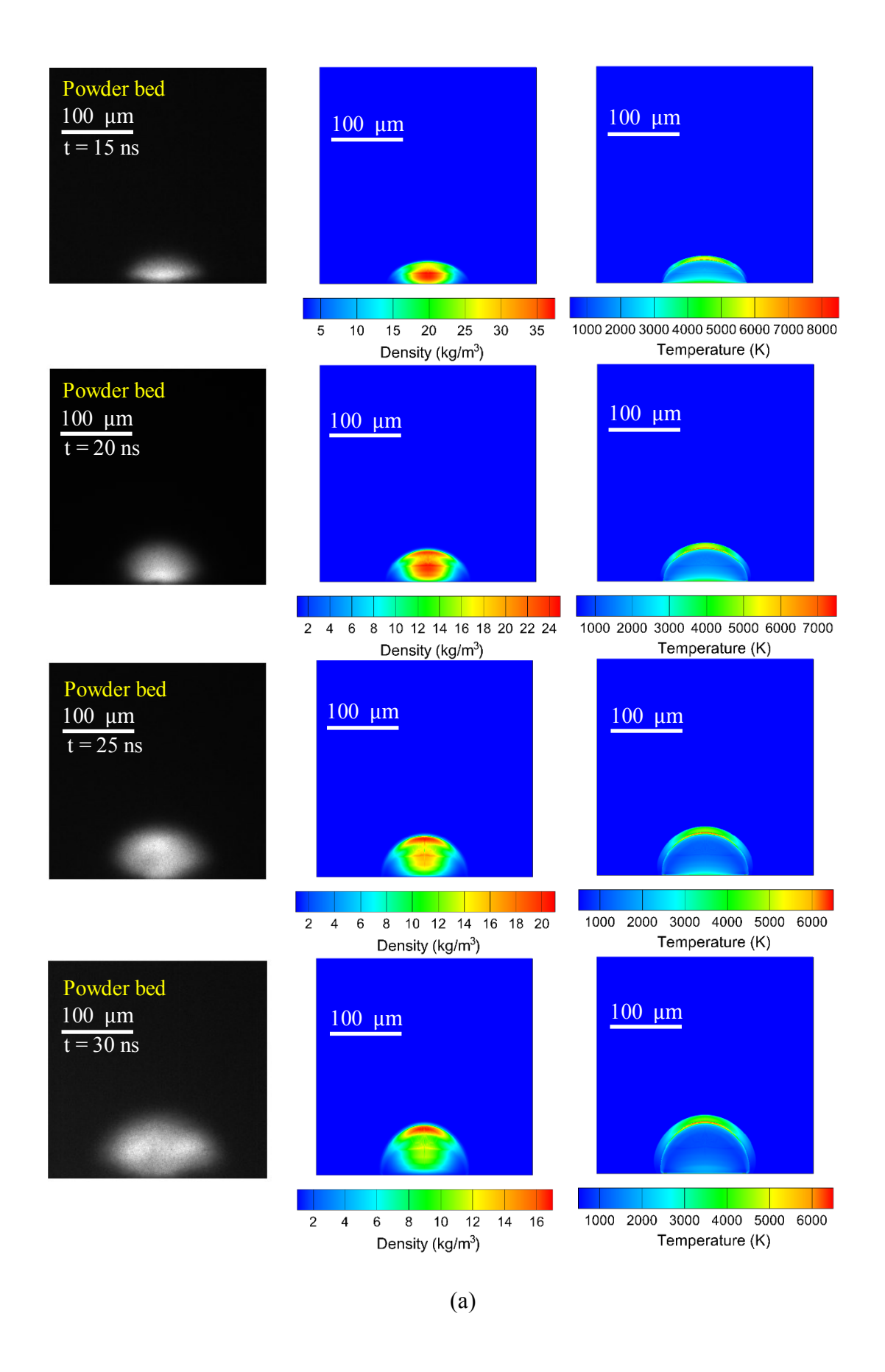


Figure 4. (a) The ICCD images (Column 1) in comparison with the model-predicted contour plots for the cobalt vapor density (Column 2) and the gaseous phase temperature (Column 3) for nanosecond laser irradiation of a bulk cobalt target. (b) The plume top front locations deduced from the experiment (ICCD images) versus those from the model simulation.

Figure 5a compares the model predictions with the ICCD images for plasma plume generated by laser irradiation of the cobalt powder bed. The figure has demonstrated that the plume top front locations shown in the ICCD images at the multiple moments given in the figure have reasonably good agreements with the model-predicted top front locations of the gaseous phase high-T (temperature) region. This is also demonstrated in Fig.5b, which gives the plume top front locations deduced from the experiment (ICCD images) versus those from the model simulation. Both the ICCD images and the model-predictions show a rapid expansion of the plume in the given period. As shown later, the peak temperature of the powder bed surface in the simulation result is still below the cobalt thermodynamic critical temperature [49]. Hence, the reasonably good agreement demonstrated in Fig.5 has reasonably supported the hypothesis posed in this study under the conditions investigated, that is, a short nanosecond laser pulse-induced plasma evolution from a metallic micro-powder bed below the critical temperature can be reasonably well described by solving gas dynamic equations in the gaseous phase together with solving the heat transfer equation in the powder bed condensed phase, where the coupling is via the Knudsen layer relations for vaporization from the surface of the condensed phase. It should also be noted that for the situations in Figs.4 and 5, the high-temperature air region, if exists, has a very small thickness (typically only a few microns or less). Hence, only the cobalt vapor density contours are shown in the figures.



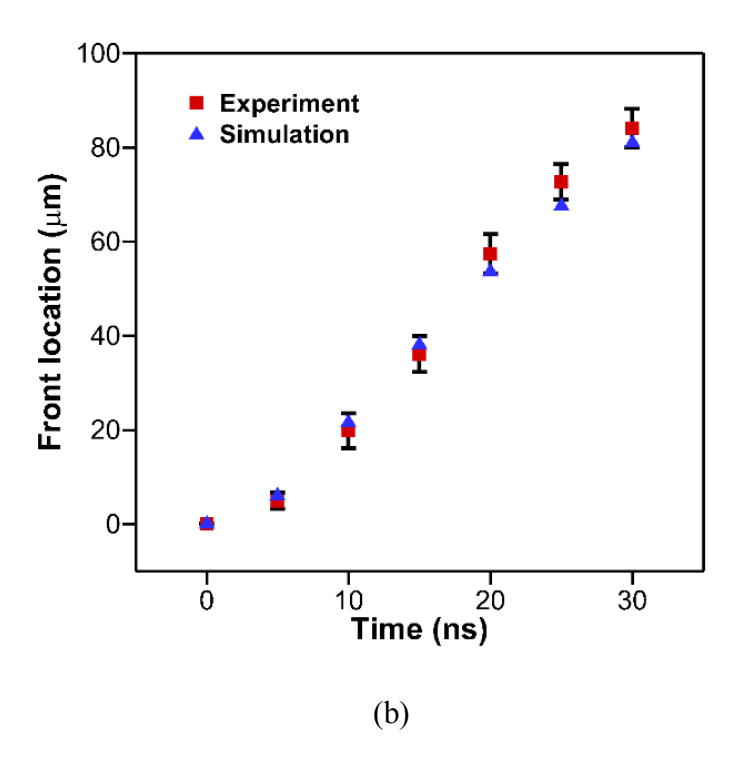


Figure 5. (a) The ICCD images (Column 1) in comparison with the model-predicted contour plots for the cobalt vapor density (Column 2) and the gaseous phase temperature (Column 3) for nanosecond-pulsed laser interaction with a cobalt micro-powder bed. (b) The plume top front locations deduced from the experiment (ICCD images) versus those from the model simulation.

Next, the model simulation results will be used to reveal the differences between the plasma plume evolutions (and related physical processes) for the powder bed and those for the bulk metal target, induced by the nanosecond laser pulse irradiation.

In Figure 6, the model-calculated contour plots for the gaseous phase temperature and the cobalt vapor density at t=30 ns for the powder bed and those for the bulk metal target are placed together for a more clear comparison. The figure has demonstrated that the high temperature gaseous phase region and the cobalt vapor region for the powder bed situation are obviously larger. The spatially peak gaseous phase temperature and the peak vapor density in the contour plots for the powder bed situation exceed ~ 6000 K and ~ 16 kg/m³, respectively. On the other hand, the peak gaseous phase temperature and the peak vapor density in the contour plots for the bulk metal situation are less than ~ 6000 K and ~ 10 kg/m³, respectively. These comparison results are consistent with what has been suggested by the in-situ time-resolved ICCD images as discussed earlier.

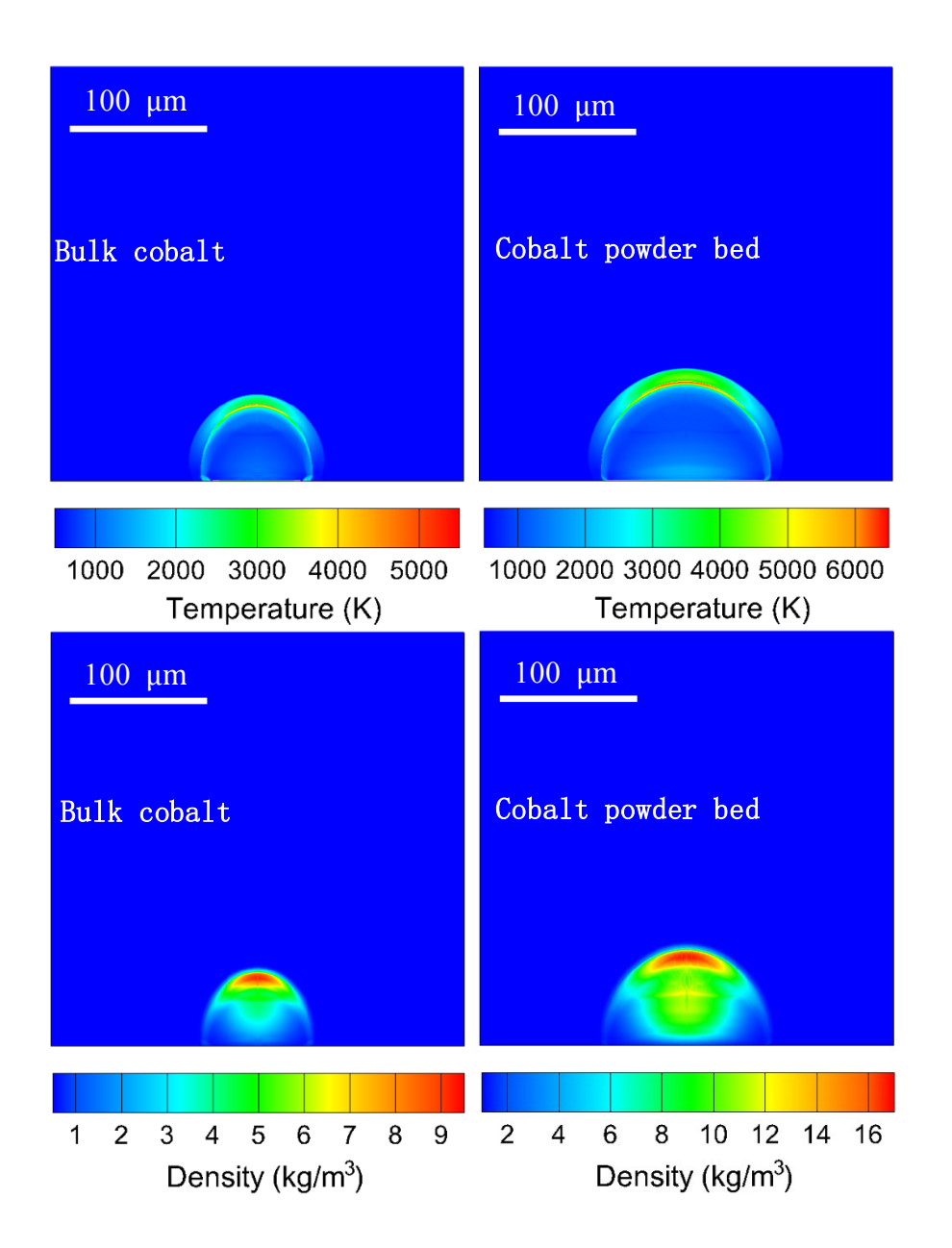


Figure 6. The model predictions for the gaseous phase temperature (Row 1) and the cobalt vapor density (Row 2) at t = 30 ns for nanosecond-pulsed laser irradiation of a bulk cobalt target (Column 1) and a cobalt powder bed (Column 2) (the laser pulse begins at t = 0).

Figure 7a and b show the temperature histories at different locations of the condensed phase surface for nanosecond-pulsed laser irradiation of the bulk cobalt target and those for the cobalt powder bed, respectively. At each given location, the temperature first increases and reaches a peak value and then drops with time. For the same surface location, the peak temperature for the powder bed surface is obviously higher than that for the bulk cobalt surface. For example, the peak surface temperatures in time for the powder bed are \sim 9416 K, \sim 8340 K and \sim 5070 K at r = 0, 25 and 50 µm, respectively, versus 7917 K, and ~5914 K, and ~1411 K, respectively, for the bulk cobalt. The cobalt thermodynamic critical temperature is ~10384 K [49]. Hence, the condensed phase peak temperatures in both simulated cases are still lower than the critical temperature (mostly lower than ~90% of the critical temperature). Figure 7c and d show the temperature distributions at the condensed phase surface in the r direction at t = 5, 20 and 30 ns for the bulk cobalt and the cobalt powder bed situations, respectively. The spatially peak temperature at each moment for the powder bed is still obviously higher than that for the bulk metal. It is expected that one important reason for the higher temperature for the cobalt powder bed surface should be that its thermal conductivity is lower than the conductivity of the bulk cobalt. The slower heat transfer in the condensed phase can help drive its surface temperature to higher values. Due to the higher surface temperatures, the surface vaporization is stronger for the powder bed than that for the bulk metal. This has led to a plasma plume with overall higher temperatures and densities for the powder bed situation in the given simulated period.

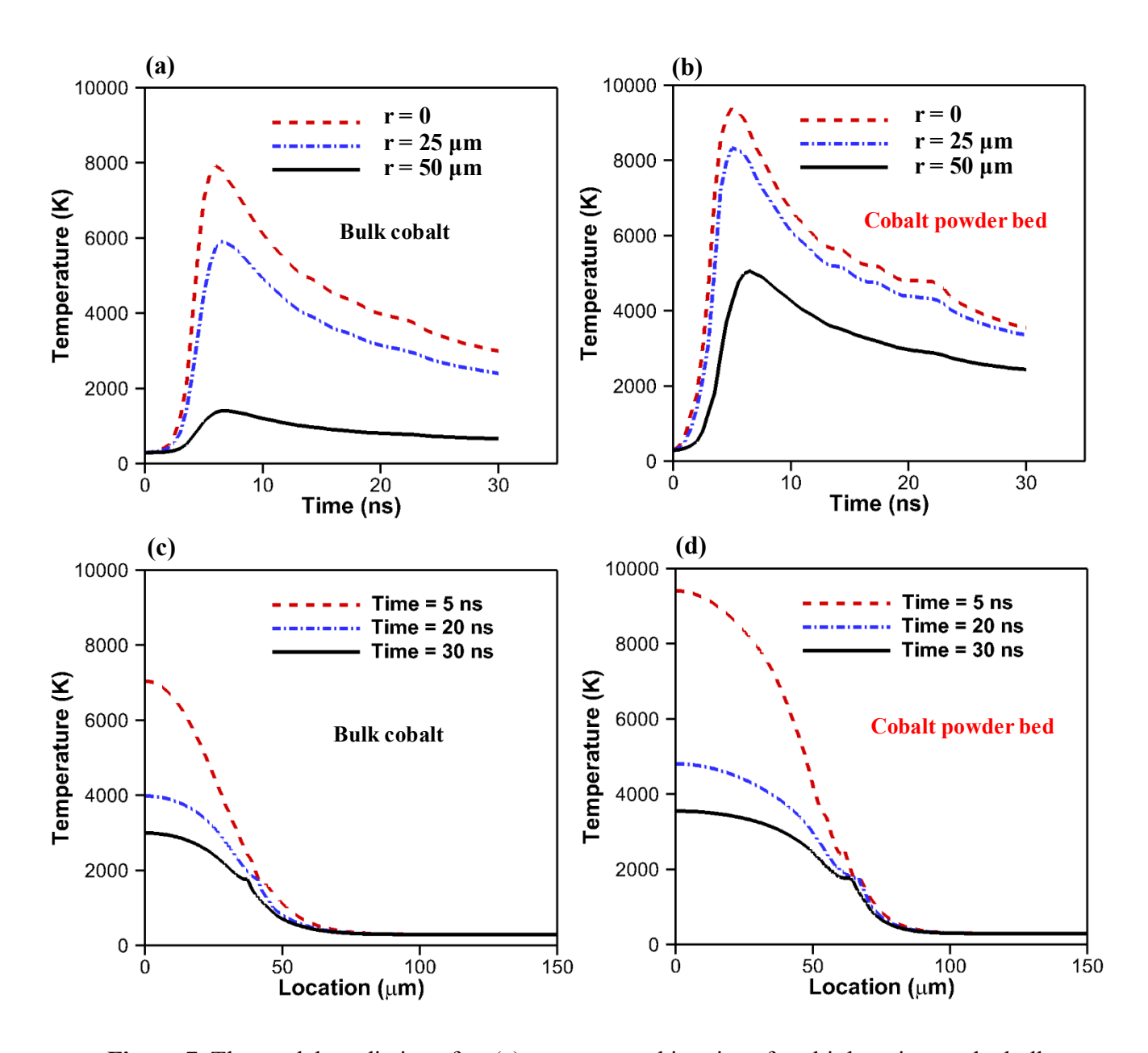


Figure 7. The model predictions for: (a) temperature histories of multiple points at the bulk cobalt target surface, (b) at the cobalt powder bed surface, (c) temperature distributions in the r direction at the bulk cobalt target surface and (d) at the cobalt powder bed surface.

Figure 8 shows the model-predicted accumulated surface-vaporized mass from the cobalt powder bed versus that from the cobalt bulk target. Compared with that for the bulk cobalt, the significant vaporization from the cobalt powder bed starts a litter earlier (\sim 3.5 ns versus \sim 4.5 ns for bulk), and the total mass vaporized by t = 20 ns is around \sim 3×10⁻¹² kg, more than \sim 6 times that for the bulk target. This should be due to the overall higher surface temperature for the cobalt powder bed. The larger amount of vaporized material is expected to be one important reason for the longer lifetime of a visible plume on the ICCD images for the powder bed than that for the bulk cobalt, as shown in Fig. 3. For both the bulk target and the powder bed, most of the vaporization (in terms of vaporized mass) occurs before t = 10 ns, indicating the short \sim 4-ns FWHM duration laser pulse has induced a very rapid vaporization.

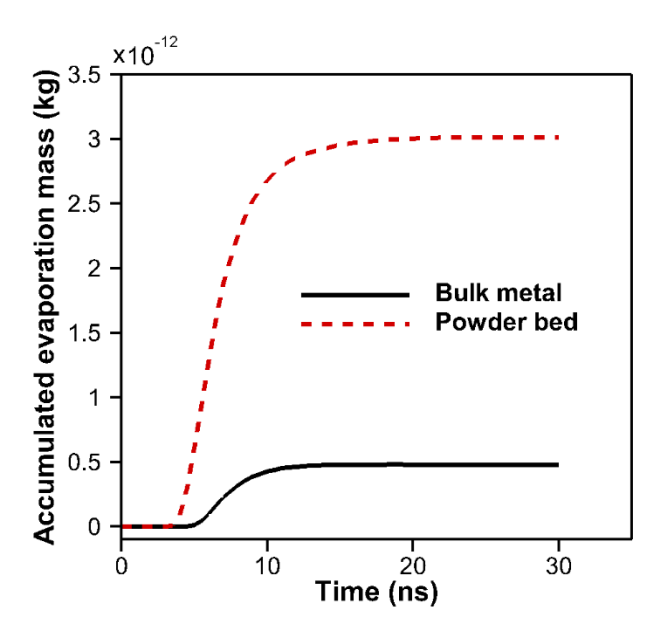


Figure 8. The model-predicted total accumulated surface-vaporized mass for nanosecond-pulsed laser irradiation of a bulk cobalt target and a cobalt powder bed.

Figure 9 gives the model-calculated total pressure that is exerted onto the condensed phase surface due to the gaseous phase pressure and velocity right above the Knudsen layer. Figure 9a and b show the total pressure histories at r = 0 and 25 µm for the bulk cobalt and the cobalt powder bed, respectively. It can be seen that for the powder bed situation the peak pressure in time is ~491 and ~ 267 MPa at r = 0 and 25 μ m, respectively, which is much higher than those for the bulk cobalt (~204 MPa and ~32 MPa at r = 0 and 25 μ m, respectively). The pressure FWHM duration is very short, which is only ~ 3.5 ns at r = 0 for the powder bed. Figure 9c and d show the pressure versus r at different moments, for the cobalt bulk target and powder bed, respectively. It can be seen that the pressure decreases very quickly with r. For example, at t = 5 ns, for the powder bed situation the pressure has the spatially peak value at r = 0 (laser spot center), and the pressure drops to 10% of the peak at $r = 41 \mu m$. The pressure drop with r is even faster for the bulk cobalt, where the pressure drops to 10% of the spatial peak value at $r = \sim 21.5 \mu m$, less than half of the laser spot radius. In summary, under the conditions investigated, the plasma plume has generated a pressure pulse with a very high transient peak magnitude, but a short duration, onto the powder bed surface. The pressure decreases quickly with r, but the high-pressure region radius is still much larger than that for the bulk cobalt.

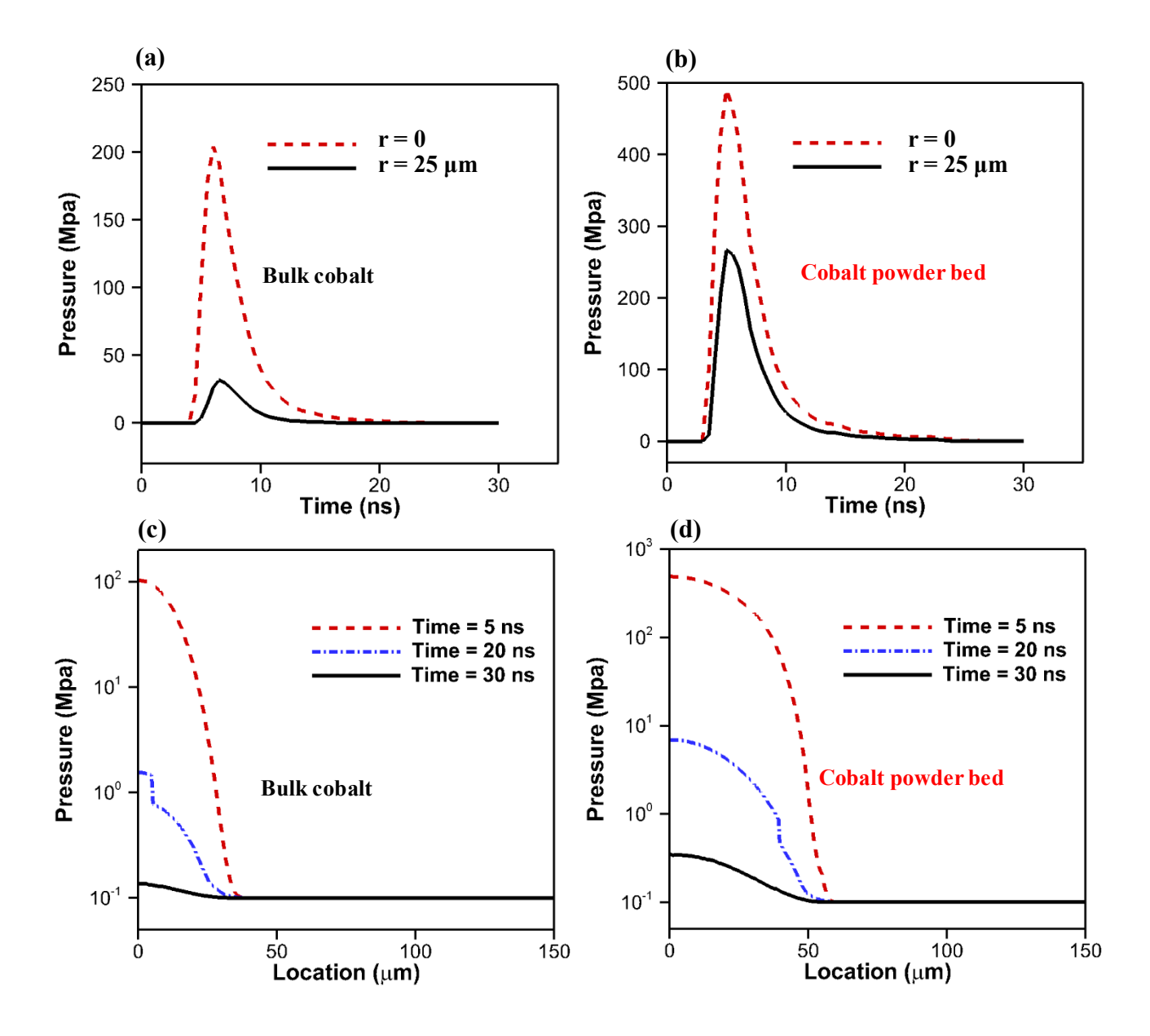


Figure 9. The model predictions for: (a) histories of the total pressure $(p + \rho_{vap}U_z^2)$ exerted on the bulk cobalt target surface at different points, (b) histories of the total pressure on the cobalt powder bed surface, (c) the total pressure distributions in the r direction at the bulk cobalt target surface and (d) at the cobalt powder bed surface.

It should be noted that the gas dynamic equations (Eq.(3)) do not consider the possible diffusion of vapor into the ambient air (although small diffusion could be numerically generated when they are numerically solved). It is believed that this has not caused any significant inaccuracy in the simulation results because the model calculations in this paper are mainly for the short period of t = 0 to 30 ns where such diffusion, if occurs, should not be very significant. This is also consistent with the reasonably good model-experiment agreements shown in Figs.4 and 5. The simulation results show that the high temperatures and the plasma-induced high pressures for the surface of the target (a bulk metal or a powder bed) mainly exist for the first \sim 30-ns period, which is thus the major focus of the modeling study in this paper. It should also be noted that the properties and evolutions of plasma induced by nanosecond laser pulse interaction with a powder bed may vary with the laser and powder bed parameters.

The modeling results in this paper indicate that nanosecond laser-generated plasma can lead to a large pressure pulse on the surface of the powder bed and hence could significantly influence the powder sintering process. The significance of nanosecond laser-induced plasma has been clearly demonstrated in the authors' previous experimental study on nanosecond laser sintering of cobalt powder with a nominal particle size of ~1.6 µm [9]. Ref.[9] shows that if low-intensity, ~200-ns duration laser pulses that do NOT generate an obvious plasma plume are used, the sintered region shows significant balling and is highly porous. On the other hand, if each ten low-intensity, ~200-ns laser pulses are followed by one high-intensity, ~4-ns laser pulse that can induce plasma, the sintered region shows much less balling and appears much more densified,

which should be due to the plasma-induced pressure pulse (please read [9] for more details). The plasma model in this paper provides a useful theoretical tool to help calculate or estimate the plasma-induced pressure due to nanosecond laser interaction with a metallic micro-powder bed. In its applicable range, it can help the understanding of related laser sintering results and/or the selection of nanosecond laser parameters to achieve the desired plasma-induced pressure impact.

The model in this study treats the powder bed as a continuum medium without explicitly simulating the evolutions of individual particles. The good model-experiment agreements shown in this paper suggest that the simplified modeling approach should be reasonably accurate to simulate the early-stage plasma evolution under the condition studied. A model explicitly simulating individual particle evolutions can give more physical details, but would have an extremely high computational cost considering that the particles in this work have a small nominal size of only ~1.6 µm and thus even a very small domain would have a large number of particles. Additive manufacturing models describing individual particles are reported in the literature, such as Refs. [50, 51], where the models are not for nanosecond laser-induced plasma and the involved particle sizes are much larger than that in this paper. The model in this paper would be improved if the evolutions of individual particles could be explicitly considered. Certainly, this will involve a significant computational cost challenge.

5. Conclusions

Short-pulsed lasers (e.g., nanosecond lasers) possess potential advantages in laser sintering, particularly laser micro sintering. At a sufficiently high intensity, a nanosecond laser pulse can generate a plasma plume from its irradiated metallic powder bed surface. The plasma plume evolution, such as the pressure it generates on the surface of the powder bed, may significantly influence the sintering process in the powder bed. However, physics-based modeling work for plasma generated by nanosecond laser interaction with a metallic micro-powder bed has been seldomly reported in literatures according to the knowledge of the authors'.

Such modeling work has been presented in the current paper for the interaction of a ~4-ns laser pulse with a cobalt micro-powder bed, integrated with time-resolved plasma imaging work using an ICCD camera with nanosecond scale gate widths for the model validation. Under the conditions studied in this modeling-experiment integrative work, the following has been found:

- (1) The model-predicted high-temperature region top front locations for the gaseous phase agree reasonably well with the top front locations of the plume shown in the ICCD-captured images for laser-induced plasma plume from both a bulk cobalt target and a cobalt powder bed for the given period in Figs. 4 and 5.
- (2) The reasonably good model-experiment agreements have supported the hypothesis under the conditions studied that: a short nanosecond laser pulse-induced plasma evolution from a metallic micro-powder bed below the thermodynamic critical temperature can be reasonably well described by solving gas dynamic equations in the gaseous phase together with solving the heat transfer equation in the powder bed condensed phase, where the coupling is via the

Knudsen layer relations for vaporization from the surface of the condensed phase. This tested hypothesis is useful new knowledge to the field, which can help guide the modeling of nanosecond laser-induced plasma from a powder bed under similar conditions.

- (3) The ICCD images show that in comparison with the nanosecond laser-induced plasma plume from the bulk cobalt, the plume from the cobalt powder bed expands faster in the period $t = \sim 10$ to ~ 30 ns, has higher apparent brightness levels on the images for $t = \sim 35$ to ~ 45 ns, and remains visible on the ICCD images for a much longer time.
- (4) The model simulations for t = 0 to 30 ns show that compared with the situation for the bulk cobalt, the nanosecond-pulsed laser irradiation of the cobalt powder bed, due to the powder bed's lower effective thermal conductivity, can induce obviously higher condensed phase surface temperatures, and thus more significant surface vaporization, and typically higher plasma peak temperatures and densities in the studied period. These are consistent with the aforementioned in-situ imaging results.
- (5) The nanosecond laser-induced plasma can produce a total pressure pulse that has a very high transient peak magnitude of ~491 MPa, but a very short duration, on the powder bed surface.

 The pressure decreases quickly with r; but the radius of the high-pressure region is still much larger than that for the bulk cobalt.

CRediT authorship contribution statement

Hanyu Song: Data curation, formal analysis, investigation, methodology, software, validation, visualization, writing-original draft, writing – review & editing.

Weidong Liu: investigation, methodology, writing – review & editing.

Benxin Wu: Conceptualization, formal analysis, funding acquisition, investigation, methodology, project administration, supervision, writing-original draft, writing – review & editing.

Declaration of Competing Interest

The authors declare the following financial interests/personal relationships which may be considered as potential competing interests: Benxin Wu has patent "Processes and systems for double-pulse laser micro sintering" (patent application number: 16/427,638) pending to Assignee: Purdue Research Foundation.

Acknowledgment

This material is based upon work supported by the National Science Foundation under Grant No. CMMI 1728481. The grantee university of the NSF award is Purdue University, which is located at the city of West Lafayette in the state of Indiana, USA. Prof. Benxin Wu, who is the corresponding author of this paper, is also the inventor of the following patent application filed that is related to laser micro sintering: Benxin Wu, inventor; Purdue Research Foundation, assignee, "Processes and systems for double-pulse laser micro sintering", United States patent application, for which the application number is 16/427,638 and the filing date is 05/31/2019 (the relevant provisional patent application has a filing date of 07/03/2018 and an application number of 62693684).

List of References

- 1. J.P. Kruth, P. Mercelis, J. Van Vaerenbergh, L. Froyen, M. Rombouts, Binding mechanisms in selective laser sintering and selective laser melting, Rapid Prototyping Journal, 11 (2005) 26-36.
- 2. Y. Wang, J. Shi, S. Lu, Y. Wang, Selective laser melting of graphene-reinforced Inconel 718 superalloy: evaluation of microstructure and tensile performance, Journal of Manufacturing Science and Engineering, 139 (2017) 041005.
- 3. C.Y. Yap, C.K. Chua, Z.L. Dong, Z.H. Liu, D.Q. Zhang, L.E. Loh, S.L. Sing, Review of selective laser melting: Materials and applications, Applied Physics Reviews, 2 (2015) 041101.
- 4. P. Fischer, M. Locher, V. Romano, H.P. Weber, S. Kolossov, R. Glardon, Temperature measurements during selective laser sintering of titanium powder, International Journal of Machine Tools and Manufacture, 44 (2004) 1293-1296.
- 5. L. Caprio, A.G. Demir, B. Previtali, Influence of pulsed and continuous wave emission on melting efficiency in selective laser melting, Journal of Materials Processing Technology, 266 (2019) 429-441.
- 6. P. Regenfuss, A. Streek, L. Hartwig, S. Klötzer, Th. Brabant, M. Horn, R. Ebert, H. Exner, Principles of laser micro sintering, Rapid Prototyping Journal, 13 (2007) 204-212.
- 7. A. Streek, P. Regenfuss, R. Ebert, H. Exner, Laser micro sintering—a quality leap through improvement of powder packing, 2008 International Solid Freeform Fabrication Symposium.
- 8. H. Song, Z. Kang, Z. Liu, B. Wu, Experimental study of double-pulse laser micro sintering: A novel laser micro sintering process, Manufacturing letters, 19 (2019) 10-14.
- 9. W. Liu, H. Song, B. Wu, H. You, Double-pulse laser micro sintering: Experimental study and mechanism analysis aided by in-situ time-resolved temperature measurements, Journal of Manufacturing Processes, 69 (2021) 191-203.
- 10. Y. Zhou, S. Tao, B. Wu, Backward growth of plasma induced by long nanosecond laser pulse ablation, Applied Physics Letters, 99 (2011) 051106.
- 11. S. Tao, Y. Zhou, B. Wu, Y. Gao, Infrared long nanosecond laser pulse ablation of silicon: integrated two-dimensional modeling and time-resolved experimental study, Applied Surface Science, 258 (2012) 7766–7773.
- 12. D. Cheng, H. Zhu, L. Ke, Investigation of plasma spectra during selective laser micro sintering Cu-based metal powder, Rapid Prototyping Journal, 19/5 (2013) 373-382.
- 13. S.G. Demos, R.A. Negres, R.N. Raman, N. Shen, A.M. Rubenchik, M.J. Matthews, Mechanisms governing the interaction of metallic particles with nanosecond laser pulses, Optics Express, 24 (2016) 7792-7815.

- 14. X.L. Li, Y.J. Li, S.T. Li, M.J. Zhou, L.W. Chen, J. Meng, D.B. Qian, J. Yang, S.F. Zhang, Y. Wu, X.W Ma, Steplike behavior in grain-size-dependent optical emission of plasma induced by laser-ablating granular material, Physical Review Applied, 16 (2021) 024017.
- 15. P. Bidare, L. Bitharas, R.M. Ward, M.M. Attallah, A.J. Moore, Fluid and particle dynamics in laser powder bed fusion, Acta Materialia, 142 (2018) 107-120.
- 16. B. Xiao, Y. Zhang, Marangoni and buoyancy effects on direct metal laser sintering with a moving laser beam, Numerical Heat Transfer, Part A: Applications, 51 (2007) 715-733.
- 17. A.V. Gusarov, I. Smurov, Thermal model of nanosecond pulsed laser ablation: Analysis of energy mass transfer, J. Appl. Phys., 97 (2005) 014307.
- 18. S.H. Jeong, R. Greif, R.E. Russo, Laser heating of metal targets including the influence of the background pressure, Proc. of the ASME Heat Transf. Division, 351 (1997) 63-73.
- 19. F.P. Incropera, D.P. Dewitt, T.L. Bergman, A.S. Lavine, Fundamentals of Heat and Mass Transfer, Wiley, Hoboken, NJ, 2007.
- 20. A.V. Gusarov, A.G. Gnedovets, I. Smurov, Gas dynamics of laser ablation: Influence of ambient atmosphere, J. Appl. Phys., 88 (2000) 4352-4364.
- 21. V. Ankudinov, G.A. Gordeev, M.D. Krivilyov, Numerical simulation of heat transfer and melting of Fe-based powders in SLM processing, In IOP Conference Series: Materials Science and Engineering 192 (2017) 012026.
- 22. The Iron Triad: Iron, Cobalt, and Nickel. (Last updated: August 25, 2020). Accessed on August 28, 2021, from https://chem.libretexts.org/@go/page/24345
- 23. Thermal Properties of Metals, Conductivity, Thermal Expansion, Specific Heat. https://www.engineersedge.com/properties_of_metals.htm (accessed on August 28, 2021).
- 24. A.H. Fleitman, R.B. Herchenroeder, J.G.Y. Chow, Cobalt-base alloys for use in nuclear reactors, Nuclear Engineering and Design, 15 (1971) 345-62.
- 25. D.S. Smith, A. Alzina, J. Bourret, B. Nait-Ali, F. Pennec, N. Tessier-Doyen, K. Otsu, H. Matsubara, P. Elser, U.T. Gonzenbach, Thermal conductivity of porous materials, Journal of Materials Research, 28 (2013) 2260-2272.
- 26. F.L. Pedrotti, L.S. Pedrotti, L.M. Pedrotti, Introduction to Optics, Pearson Prentice Hall, 2007.
- 27. S. Gurlui, M. Agop, P. Nica, M. Ziskind, C. Focsa, Experimental and theoretical investigations of a laser-produced aluminum plasma, Phys. Rev. E., 78 (2008) 026405.
- 28. J.C. Tannehill, D.A. Anderson, R.H. Pletcher, Computational Fluid Mechanics and Heat Transfer, second ed., Taylor and Francis, Washington, DC, 1997.
- 29. B. Wu, Y.C. Shin, Modeling of nanosecond laser ablation with vapor plasma formation, J. Appl. Phys., 99 (2006) 084310.

- 30. L. Spitzer, Physics of Fully Ionized Gases, Interscience Publishers, Inc., New York, 1956.
- 31. M. Mitchner, C.H. Kruger, Partially Ionized Gases, Wiley, New York, 1973.
- 32. Y.B. Zel'dovich, Y.P. Raizer, Physics of Shock Waves and High-temperature Hydrodynamic Phenomena, Academic Press, New York and London, 1966-1967.
- 33. M.R. Zaghloul, M.A. Bourham, J.M. Doster, A simple formulation and solution strategy of the Saha equation for ideal and nonideal plasmas, Journal of Physics D: Applied Physics, 33 (2000) 977-984.
- 34. Oxygen Electron Affinity Electronegativity Ionization Energy of Oxygen, https://www.nuclear-power.com/oxygen-affinity-electronegativity-ionization/ (accessed on September 4, 2021)
- 35. Nitrogen Electron Affinity Electronegativity Ionization Energy of Nitrogen, https://www.nuclear-power.com/nitrogen-affinity-electronegativity-ionization/ (accessed on September 4, 2021)
- 36. K. Kadoya, N. Matsunaga, A. Nagashima, Viscosity and thermal conductivity of dry air in the gaseous phase, Journal of Physical and Chemical Reference Data, 14 (1985) 947-970.
- 37. X.D. Liu, S. Osher, Convex ENO high order multi-dimensional schemes without field by field decomposition or staggered grids, J. Comput. Phys., 142 (1998) 304 330.
- 38. C.J. Knight, Transient vaporization from a surface into vacuum, AIAA J., 20 (1982) 950-954.
- 39. C.J. Knight, Theoretical modeling of rapid surface vaporization with back pressure, AIAA J., 17 (1979) 519-523.
- 40. S.I. Anisimov, Vaporization of metal absorbing laser radiation, Sov. Phys. JETP, 27 (1968) 182-183.
- 41. A. Peterlongo, A. Miotello, R. Kelly, Laser-pulse sputtering of aluminum: Vaporization, boiling, superheating, and gas-dynamic effects, Phys. Rev. E., 50 (1994) 4716-4727.
- 42. A.F. Guillermet, Critical evaluation of the thermodynamic properties of cobalt, International Journal of Thermophysics, 8 (1987) 481-510.
- 43. Z. Li, S. Bigdeli, H. Mao, Q. Chen, M. Selleby, Thermodynamic evaluation of pure Co for the third generation of thermodynamic databases, Physica Status Solidi (b), 254 (2017) 1600231.
- 44. Y. Terada, K. Ohkubo, T. Mohri, T. Suzuki, Thermal conductivity of cobalt-base alloys, Metallurgical and Materials Transactions, 34A (2003) 2026-2028.
- 45. M.J. Assael, K.D. Antoniadis, W.A. Wakeham, M.L. Huber, H. Fukuyama, Reference correlations for the thermal conductivity of liquid bismuth, cobalt, germanium, and silicon, Journal of Physical and Chemical Reference Data, 46 (2017) 033101.

- 46. A.C. Yu, T.M. Donovan, W.E. Spicer, Optical properties of cobalt, Physical Review, 167 (1968) 670-673.
- 47. E. Siegel, Optical reflectivity of liquid metals at their melting temperatures, Physics and Chemistry of liquids, 5 (1976) 9-27.
- 48. D. R. Lide (ed), CRC Handbook of Chemistry and Physics. CRC Press. Boca Raton, Florida, Internet version 2005; Section 10, Atomic, Molecular, and Optical Physics; Ionization Potentials of Atoms and Atomic Ions.
- 49. H. Hess, E. Kaschnitz, G. Pottlacher, Thermophysical properties of liquid cobalt, High Pressure Research, 12 (1994) 29-42.
- 50. W. Yan, W. Ge, Y. Qian, S. Lin, B. Zhou, W.K. Liu, F. Lin, G.J. Wagner, Multi-physics modeling of single/multiple-track defect mechanisms in electron beam selective melting, Acta Materialia. 134 (2017) 324-33.
- 51. H. Chen, W. Yan, Spattering and denudation in laser powder bed fusion process: Multiphase flow modelling, Acta Materialia, 196 (2020) 154-67.

Table 1. Main cobalt properties employed in the simulations by the model [24, 42-48].

Properties*	Value or Source	Unit
Melting point [24]	1768 (converted from 1495 °C in [24])	K
Normal boiling point [24]	3173 (converted from 2900 °C in [24])	K
Latent heat of melting [24]	58.4	cal/g
Latent heat of vaporization [24]	1500	cal/g
Bulk solid density [24]	8850	kg/m³
Bulk liquid density [42]	7750	kg/m³
Solid specific heat [43]	430 (averaged from the two heat capacity values at 298 K given in Table 5 of [43])	J/kg·K
Liquid specific heat [43]	690 (approximately converted from 40.5 J/mol· K that is from [43])	J/kg·K
Bulk solid thermal conductivity	Based on a linear interpolation utilizing the first low-T data point as well as the data point at T = 1000 K from Fig.3 of [44] for pure cobalt (for solid at T>1000 K, the value at 1000 K is utilized)	
Bulk liquid thermal conductivity	Table 6 of [45] (for liquid at T > 1950 K or T<1800 K, the value for 1950 K or 1800 K is utilized, respectively)	
Solid-state complex index of refraction	Based upon Figure 6 in [46]	
Liquid-state complex index of refraction	Based on Table III of [47] (the value at the melting temperature for $\lambda = 1.06 \mu m$ has been utilized)	
Cobalt ionization energies	From Ref. [48]	

^{*}The effective powder-bed medium thermal conductivity and density are determined using the bulk cobalt properties in the way as described in the text of this paper.